

## The Nanofluidic Confinement Apparatus: Studying confinement dependent nanoparticle behavior and diffusion

Stefan Fringes,<sup>1, a)</sup> Felix Holzner,<sup>1, b)</sup> and Armin W. Knoll<sup>1, c)</sup>

*IBM Research - Zurich, Säumerstr. 4, 8803 Rüschlikon,  
Switzerland*

(Dated: 17 January 2017)

We present a versatile setup for investigating the nanofluidic behavior of nanoparticles as a function of the gap distance between two confining surfaces. The setup is designed as an open system which operates with small amounts of dispersion of  $\approx 20 \mu\text{l}$ , permits the use of coated and patterned samples, and allows high-numerical-aperture microscopy access. Piezo elements enable 5D relative positioning of the surfaces. We achieve a parallelization of less than 1 nm vertical deviation over a lateral distance of  $10 \mu\text{m}$ . The vertical separation is tunable and detectable with subnanometer accuracy down to direct contact. At rest, the gap distance is stable on a nanometer level. Using the tool we measure the vertical position termed height and the lateral diffusion of 60 nm charged Au nanospheres as a function of confinement between a glass and a polymer surface. Interferometric scattering detection results in sub 10 nm vertical and sub 5 nm lateral particle localization accuracy, and a single particle illumination time below  $40 \mu\text{s}$ . We measure the height of the particles to be consistently above the gap center, corresponding to a higher charge on the polymer substrate. In terms of diffusion, we find a strong monotonic decay of the diffusion constant with decreasing gap distance. This result cannot be explained by hydrodynamic effects, including the asymmetric vertical position of the particles in the gap. Instead we attribute it to an electroviscous effect. For strong confinement of less than 120 nm gap distance, we detect an onset of sub-diffusion which can be correlated to a motion of the particles along high-gap-distance paths.

PACS numbers: 66.10.C-, 68.08.-p, 42.25.Hz

Keywords: Suggested keywords

---

<sup>a)</sup>Also at Department of Chemistry, University of Zurich.

<sup>b)</sup>Present address: SwissLitho AG, Technoparkstrasse 1, 8005 Zurich.

<sup>c)</sup>Electronic mail: ark@zurich.ibm.com.

## I. INTRODUCTION

A fundamental understanding of the motion of micro- and nano-scaled objects in nanofluidic confinement is important for many biological and technical processes such as the anomalous diffusion in cellular environments,<sup>1,2</sup> the delivery of drugs,<sup>3</sup> the formation of colloidal crystals,<sup>4,5</sup> particle sorting,<sup>6</sup> and directed self-assembly.<sup>7</sup>

Nanofluidic systems in general are characterized by spatial distances in at least one dimension of less than 100 nm. This distance range interferes with several natural length scales of particle-surface interactions<sup>8</sup>, such as the electrostatic interactions. The electrostatic interactions between charged objects and surfaces in a nanofluidic system decay approximately exponentially with separation and a characteristic length scale termed Debye length.<sup>9</sup> Experimentally, the gap-distance-dependent forces between two curved surfaces were studied in micro-rheology experiments<sup>10,11</sup> and in detail using the surface force apparatus<sup>12</sup>. However, so far, most nanofluidic experiments involving confined particles have been performed using static surfaces and fixed geometries, which do not allow the degree of confinement to be varied *in situ*.

Recently it was demonstrated that the gap-distance-dependent electrostatic forces can be exploited to achieve geometry-induced trapping and manipulation of charged nanoparticles and vesicles in nanofluidic systems.<sup>13</sup> In a follow-up experiment, it was shown that crucial information on the trapping potential can be gained by using an AFM-type system and a micro-capillary to adjust the gap distance.<sup>14</sup>

Another example of a strongly gap-dependent behavior is the lateral diffusion of particles in a nanofluidic gap. In microfluidic systems, it has been shown that the theoretical predictions of hydrodynamically hindered diffusion are in agreement with the measured diffusivity of microparticles.<sup>15,16</sup> However, in nanofluidic systems, a 50 – 70 % lower diffusion is observed when geometrical dimensions approach the Debye screening length<sup>17–19</sup>. The mechanisms that have been proposed to explain the increased hindrance are anomalous viscosity<sup>17</sup>, anomalous diffusion<sup>19</sup> and an electroviscous effect.<sup>18</sup>

Here we present a versatile setup that allows the distance between two parallel confining surfaces for samples of choice and a cover-glass to be adjusted and measured with nanometer accuracy. First, we describe and characterize the system, and then demonstrate its utility by measuring the behavior of 60 nm charged Au nanospheres in confinement between a glass

and a polymer surface. We first determine the height of the particles as a function of gap distance by means of their varying optical contrast. Next we determine the lateral diffusion for a range of fixed gap distances. The gap-dependent measurement allows us not only to measure the decreasing diffusion coefficients but also to determine the onset of a scale dependent diffusion induced by the roughness of the confining surfaces. A comparison with theory indicates that hydrodynamic effects alone cannot explain the behavior observed.

## II. METHOD

### A. Nanofluidic confinement apparatus

A schematic illustration of the nanofluidic confinement apparatus is shown in Fig. 1(a). The optical illumination and detection scheme is based on interferometric scattering detection (iSCAT) and was described in detail elsewhere<sup>20–23</sup>, here we just provide a brief description.

By raster scanning the focus of a 532 nm continuous-wave laser (Samba 50 mW, Cobolt), the sample area of interest is illuminated. Scanning and focusing are done by a two-axis acousto-optic deflector (DTSXY, AA Opto-Electronic), a telecentric system, and a 100 $\times$ , 1.4 numerical aperture (NA) oil-immersion objective (Alpha Plan-Apochromat, Zeiss). The reflected light is collected by the same objective, and images are captured by a high-frame-rate camera (MV-D1024-160-CL-12, Photon Focus). Typically we use a field of view of 300  $\times$  300 pixels, corresponding to an area of 33  $\times$  33  $\mu\text{m}^2$ . The imaging rate is 800 frames per second (FPS), given by the exposure time of 0.75 ms and a trigger delay of 0.5 ms, which was selected to avoid frame drops. We achieve uniform illumination using a single scan per frame and a laser line spacing of 500 nm, which is consistent with an estimated laser spot size of  $\approx 2 \mu\text{m}$ . Accordingly, a single point on the sample is scanned by  $\leq 4$  laser lines of 10  $\mu\text{s}$  duration corresponding to a total time of  $\tau_{\text{avg}} \lesssim 40 \mu\text{s}$ . During  $\tau_{\text{avg}}$  the diffusion of a 60 nm Au nanoparticle (bulk diffusivity  $D_p \approx 7 \mu\text{m}^2\text{s}^{-1}$ ) in one dimension is  $\lesssim \sqrt{2D_p\tau_{\text{avg}}} \approx 25 \text{ nm}$ , which is small compared to the laser line spacing. Thus the image taken by the camera contains information about the position of the particle averaged over a duration of  $\lesssim \tau_{\text{avg}}$ .

The mechanical part with the tunable confinement setup is mounted below the objective (see Fig. 1(b)). A schematic cross section through the center of the system is sketched

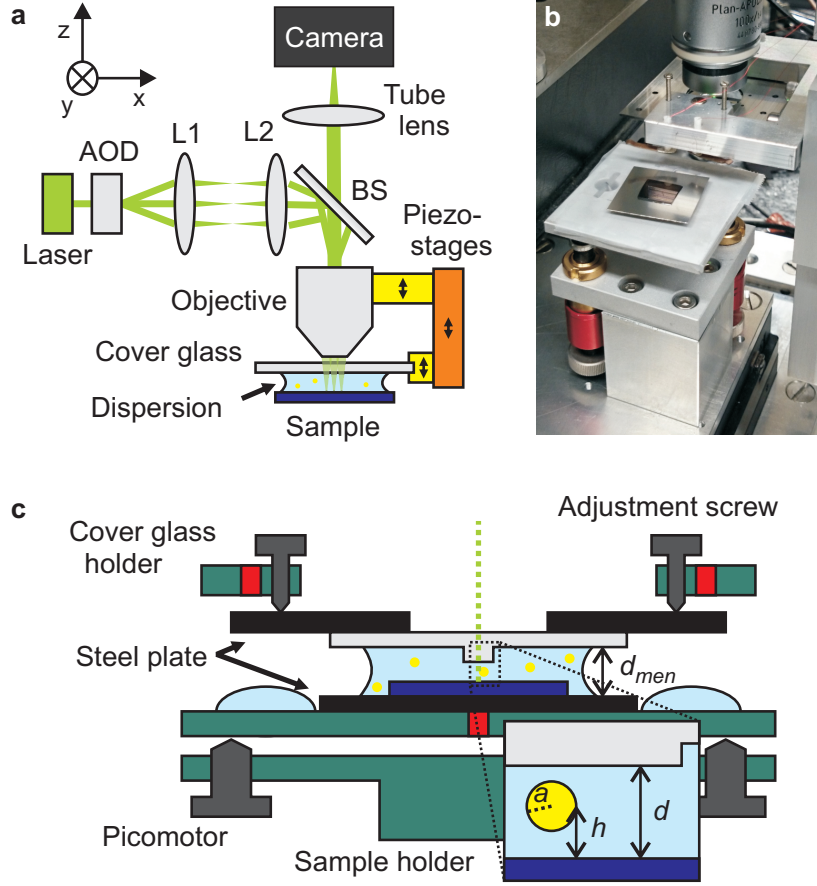


FIG. 1. (a) The optical setup consist of a laser, an acousto-optic deflector (AOD), and a telecentric system (L1 and L2) for scanned laser illumination of the sample through a beam splitter (BS), and an oil immersion objective. Two linear piezo-stages (yellow) and one coarse-positioning stage (orange) allow to fine tune the focus and the confinement independently and to access a large range of gap distances. (b) Photograph of the nanofluidic confinement apparatus. (c) Sketch of the vertical profile of the system, see text for details. The inset visualizes the nanofluidic slit with gap distance  $d$  confining a particle with radius  $a$  at height  $h$ .

in Fig. 1(c) (not to scale): A droplet of particle dispersion is confined by the cover-glass (light gray) and the sample (dark blue). The glass and the sample are both glued to steel plates (black). Magnets (red) in the aluminum holders (green) fix the position of the steel plates. Three adjustment screws are used to align the tilt of the cover-glass with respect to the focal plane of the objective. Parallelization of the substrate to the cover-glass is done by three linear piezo actuators (Picomotor, Newport). The distance of the cover-glass and

the microscope objective relative to the substrate is controlled by two linear piezo-stages ( $100\text{ }\mu\text{m}$ , Nano-OP100, Mad City Labs), which are attached to a coarse-positioning stage (MT-84, Feinmess). A mesa is etched in the cover-glass such that the area outside the mesa is recessed by  $\approx 50\text{ }\mu\text{m}$  (see next section for details). The mesa provides good optical access to the nanofluidic region and ensures that the gap distance  $d$  between the cover-glass and sample (see inset of Fig. 1(c)) can be reduced until a colloid has intimate contact to both surfaces.

A droplet volume of  $V_{\text{drop}} \geq 20\text{ }\mu\text{l}$  is required such that the dispersion overflows the sample and wets the metal holder. This geometry increases the distance at the meniscus  $d_{\text{men}}$  to approximately  $600\text{ }\mu\text{m}$  (sample thickness  $550\text{ }\mu\text{m}$ ). Therefore also the radius of curvature of the droplet is increased, resulting in a reduced Young–Laplace pressure and a high stability of the system. A water reservoir next to the central droplet (Fig. 1(c)) reduces the evaporation of the droplet in the slit and ensures system stability for several hours.

## B. Cover-glass and sample preparation

The mesa of the cover-glass (D263T borosilicate, UQG) was fabricated as follows: First, a masking layer of  $30\text{ nm}$  Cr and  $300\text{ nm}$  Au was sputtered onto the glass. Second, a photoresist (AZ4533, MicroChemicals) was spin coated and patterned by photolithography. Third, the masking layer was removed by wet etching (TechniEtch ACI2, MicroChemicals and TechniStrip Cr01, MicroChemicals) of the unprotected areas, leaving behind a central metal-resist stack defining the position of the mesa. The area around the stack was etched for  $75\text{ s}$  by concentrated hydrofluoric acid ( $49\%$  HF) to define the mesa. A mesa height of  $40\text{--}45\text{ }\mu\text{m}$  was measured with a profilometer (Dektak, Veeco), corresponding to an etch rate of  $\approx 36\text{ }\mu\text{m}/\text{min}$ , similar to the rate observed by Zhu et al.<sup>24</sup> Finally, the remaining masking layer was removed by etching, and the processed cover-glass was cleaned by peeling off a polymer layer (Red First Contact, Photonic Cleaning Technologies), in a helium plasma (Piezobrush, Relyon Plasma) for  $20\text{ s}$  and by rinsing with ultrapure water (Millipore,  $18\text{ M}\Omega\text{cm}$ ).

A  $52\text{ nm}$  thick cross-linking polymer (HM8006, JSR) was spin coated onto a silicon sample to increase adhesion for the subsequently spin coated  $175\text{ nm}$  thick poly-phthalaldehyde (PPA) film. The thicknesses were measured with AFM. The refractive indices  $n_{HM} = 1.67$  and  $n_{PPA} = 1.59$  were measured by ellipsometry.

A colloid of citrate stabilized 60 nm Au nanospheres (BBI Solutions) with a manufacturer-specified diameter of  $2a = 59.8 \pm 4.8$  and density of  $\approx 2.6 \times 10^{12}$  particles per ml was diluted 1:10 in fresh ultrapure water (Millipore, 18 M $\Omega$ cm) to reduce the ion concentration. The diluted dispersion was used within a few hours. A pH of  $6.8 \pm 0.2$ , a zeta potential of  $\zeta = -58$  mV, a specific conductivity of  $\Lambda = 11.5 \mu\text{Scm}^{-1}$ , and hydrodynamic diameter of  $2a = 62.1$  nm were measured for a 1:150 diluted dispersion using a Malvern Zetasizer. We observed a linear dependency between the conductivity and the degree of dilution, which is expected for strong electrolytes such as sodium citrate and sodium chloride. Both can be present, since the synthesis involves the reduction of chloroauric acid ( $\text{HAuCl}_4$ ) by sodium citrate ( $\text{Na}_3\text{Cit}$ ).<sup>25</sup> The citrate also functions as a capping agent, therefore we first determine the cation concentration from the conductivity measurement and then estimate an upper limit for the Debye length of  $\kappa^{-1} \approx 8.9$  nm for the 1:10 diluted colloid. In an independent measurement, we determined a larger Debye length for the same but more diluted colloid, consistent with the Debye length presented here.<sup>23</sup>

### C. Measurement of gap distance and stability of the mechanical setup

The performance of the setup is characterized by the precision achieved in controlling and detecting the gap distance. For a slit filled with aqueous dispersion, a change in gap distance leads to a change in the Young–Laplace pressure, which bends the cover-glass such that the motion of the piezo and the cover-glass are not in 1:1 correspondence. Therefore we use the interference of the light between the sample and the cover-glass as a measurement of the gap distance.

For this measurement, we have to consider light rays departing from normal incidence, because we use a high NA objective to focus and collect the light. We address this issue by determining an effective incident angle as described in detail in Ref.<sup>23</sup>. The angle is determined from a measurement of the normalized interference intensity  $I'$  as a function of the cover glass position  $z$  in air to avoid the effect of the pressure changes mentioned above, see Fig. 2 (a). The signal arises from the interference of light rays reflected by the interfaces of the glass-water-polymer-silicon stack. We have developed an optical model<sup>23</sup> based on the transfer-matrix method, that considers the focusing of a Gaussian laser-beam. The result of a fit to the data is shown as red dashed line in Fig. 2 (a). Fit parameters are the effective

incident angle  $\Theta_{\text{eff}} = 5.9^\circ$  and the phase of the signal. The phase of the signal and the first contact point at a gap distance of  $d \approx 80$  nm fixes the absolute gap distance (see red axis). The required refractive indices for silicon,  $n_{\text{Si}} = 4.14$ , and for the cover-glass,  $n_{\text{D263}} = 1.53$ , are taken from literature. To measure the gap distance in the water-filled system, we use the optical model and propagate the effective incident angle into the dielectric layers by using Snells law.

Parallelization of the surfaces is achieved by measuring the interference signal in the four corners and at the center of the illuminated area (see Fig. 2(b)): From the relative phase shift of the respective signals (see Fig. 2(c)), the tilt of the confining surfaces can be determined. By tilting the sample, the phase difference was minimized using the cross-correlation of the corner to the center signals.

The optical path difference between glass and substrate varies because of the inherent surface roughness of the contributing interfaces. This fact leads to a varying phase shift of the interference signal pixel by pixel. AFM measurements yield the following root-mean-square (RMS) roughnesses:  $S_q^{\text{D263}} \approx 0.4$  nm for the cover-glass,  $S_q^{\text{PPA}} \approx 0.3$  nm for the polymer surface and  $S_q^{\text{Si}} \approx 0.2$  nm for the silicon wafer. Since the silicon wafer is relatively flat and the refractive indices of polymer and glass are similar we approximate that all the phase differences originate from a roughness in the cover glass. The conversion from the phase shift to the gap distance is performed using the optical model mentioned above. The resulting gap distance image Fig. 2(d), reveals a remnant tilt between the two confining surfaces, which could be corrected further. Without this correction, we achieve a height difference of 3 nm over a distance of  $30 \mu\text{m}$ . The standard deviation of the plane corrected gap distance image is  $S_q^{\Delta d} \approx 0.6$  nm, which is consistent with the measured surface roughness values.

During the measurements described in the subsequent sections, thermal drift and pressure changes may lead to a deflection of the relatively compliant cover-glass. These deflections are compensated by implementing a closed-loop system, that registers changes in the background interference intensity and adjusts the height of the cover-glass to keep the intensity constant. The feedback-loop can also operate during acquisition with a frequency of 20 Hz as illustrated by the red lines in Fig. 2(e)). The blue lines indicate the measured laterally averaged gap distances for 15 s.

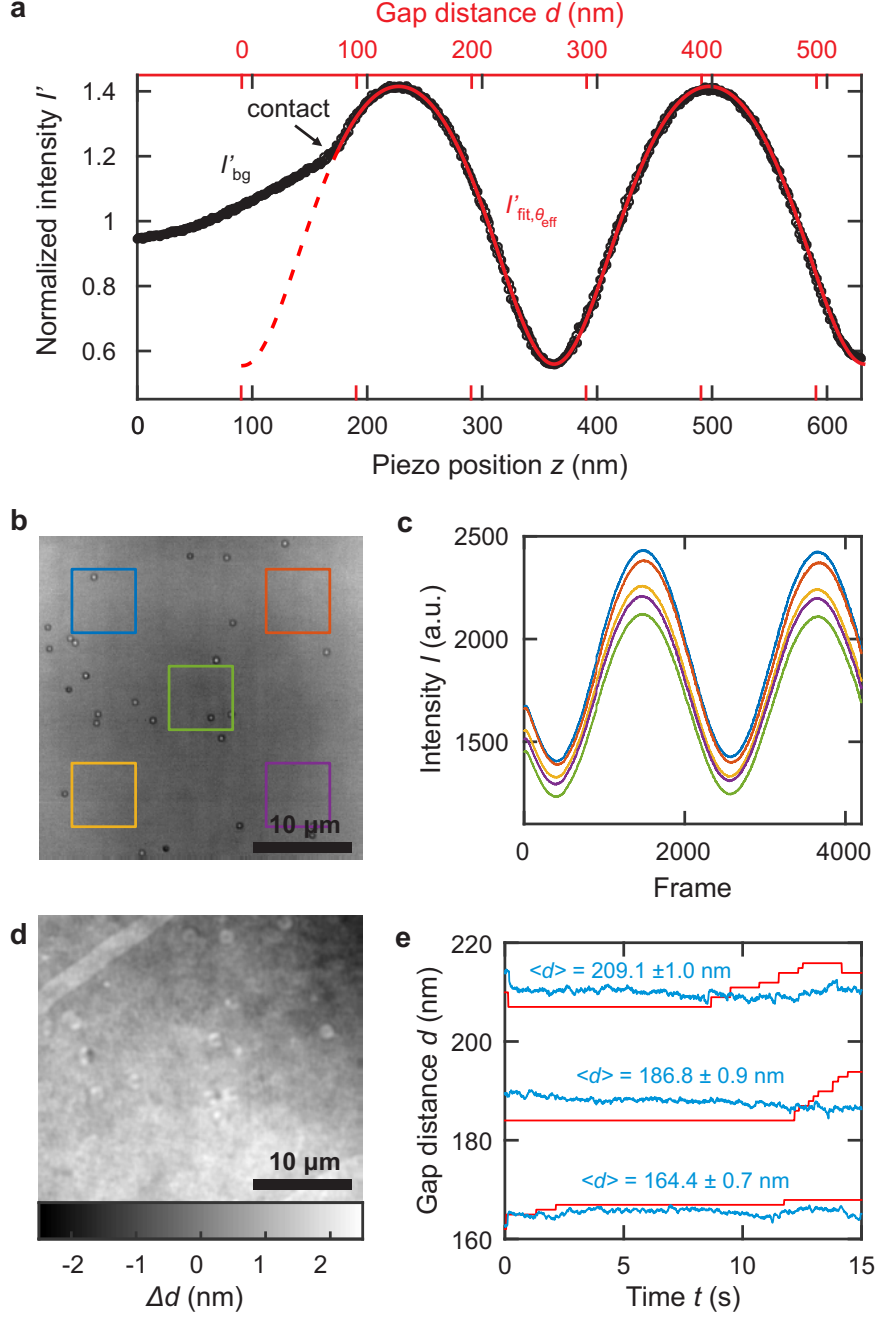


FIG. 2. (a) Measured intensity reflected from a glass-air-silicon slit (black) while the cover-glass is displaced vertically with a piezo motor. The red line depicts the result of a fit to our optical model. (b) Typical raw image of 60 nm Au nanospheres in the nanofluidic slit. (c) The median intensity captured in the areas indicated by the boxes in (b), while increasing the gap distance by 1 nm every 10th frame. (d) Effective gap distance variation  $\Delta d$  in the nanofluidic slit obtained from the local variation in optical path difference. (e) The height of the cover-glass (red) is adjusted by a feedback loop to ensure a constant gap distance (blue) during experiments.



## D. Particle localization

Radial symmetry-based tracking was used to identify the central lateral position of the nanosphere. This tracking algorithm yields similar accuracies compared to Gaussian fitting, is fast in execution, and detects any radially symmetric intensity distribution.<sup>26</sup> In particular the latter is important to detect the position at interference conditions for which the particle contrast vanishes at the center and only a diffraction ring of finite intensity is measured. We estimate an average lateral localization precision of  $\leq 5$  nm from the scatter of 35,000 detected positions obtained from 7 immobilized particles. This precision is in agreement with simulated particles<sup>26</sup> with a similar signal-to-noise ratio (SNR) of  $\approx 20$ . We like to point out that we measure the same SNR using raw images similar to that in Fig. 2 (b), but for moving particles we can reduce the fixed-pattern camera pixel noise of the background by subtracting the temporal median of the image stack. With that correction, we obtain a SNR of  $\approx 50$ , which corresponds to a localization accuracy of less than 1.5 nm.<sup>26</sup>

## III. CONFINED LATERAL DIFFUSION

In the following we first revisit briefly the existing hydrodynamic models describing confined lateral particle diffusion. According to these models, the diffusivity depends not only on the gap distance but also on the vertical position of the particles in the gap. To test these predictions, we included in our measurements described in the subsequent sections not only the diffusion but also the height of the particles in the gap.

### A. Hydrodynamic models

Following the work of Eichmann *et al.*<sup>18</sup>, we present the linear superposition (LSA) and the coherent superposition approximation (CSA) to calculate the hindered lateral diffusion in a fluidic slit. A third approximation, the matched asymptotic expansion (MAE), is not considered here as it deviates only slightly from the LSA.

The diffusion coefficient of a freely moving spherical particle obeys the Stokes–Einstein-equation

$$D_0 = \frac{kT}{6\pi\eta a}, \quad (1)$$

where  $k$  is Boltzmann's constant,  $T$  is the absolute temperature, and  $\eta$  is the dynamic viscosity of the continuous medium. The hydrodynamically hindered diffusion parallel to a single interface is conveniently given by a correction factor  $f_{||1}$ :

$$D_{||1}(h, a) = D_0 f_{||1}(h, a). \quad (2)$$

Solutions are given in terms of the dimensionless particle height,  $\omega = h/a$ , for<sup>27</sup>

$\omega > 1.1$  :

$$\begin{aligned} f_{||1}(h, a) = 1 - \frac{9}{16}\omega^{-1} + \frac{1}{8}\omega^{-3} - \frac{45}{256}\omega^{-4} - \frac{1}{16}\omega^{-5} \\ + 0.22206\omega^{-6} - 0.205216\omega^{-7} \end{aligned} \quad (3)$$

$\omega \leq 1.1$  :

$$\begin{aligned} f_{||1}(h, a) = 1 - \frac{15/8}{\ln(\omega - 1)} \\ + e^{1.80359(\omega-1)} + 0.319037(\omega - 1)^{0.2592} \end{aligned} \quad (4)$$

by Fax  n<sup>28</sup> and Goldman<sup>29</sup>, respectively. A similar approach leads to the drag-reduced diffusion in a slit<sup>30</sup>:

$$D_{||2}(h, a, d) = D_0 f_{||2}(h, a, d), \quad (5)$$

where  $d$  is the gap distance of the confining walls. Oseen suggested the LSA<sup>30</sup>

$$f_{||2}^{\text{LSA}}(h, a, d) = [f_{||1}(h, a)^{-1} + f_{||1}(d - h, a)^{-1} - 1]^{-1}, \quad (6)$$

where the drag of each wall is treated independently and the total force is given by the sum of the contributions.

Another expression, the CSA

$$\begin{aligned} f_{||2}^{\text{CSA}}(h, a, d) = [1 + S_1 + S_2 - 2S_3]^{-1} \\ S_1 = \sum_{n=0}^{\infty} (f_{||1}(nd + h, a)^{-1} - 1) \\ S_2 = \sum_{n=1}^{\infty} (f_{||1}(nd - h, a)^{-1} - 1) \\ S_3 = \sum_{n=1}^{\infty} (f_{||1}(nd, a)^{-1} - 1) \end{aligned} \quad (7)$$

includes multiple interactions of the perturbations of the pressure and velocity fields induced by each wall. The same interactions with the colloid are not included.<sup>15,31</sup>

The lateral diffusion coefficient  $D_{||2}$  can be measured from the mean squared displacement (MSD) in one of the orthogonal directions  $x$  or  $y$ . For the  $x$ -direction and a time interval  $\Delta t$ , the MSD is given by

$$\langle \Delta x^2(\Delta t) \rangle = \left\langle \frac{1}{N-1} \sum_{i=1}^{N-1} [x(t_i + \Delta t) - x(t_i)]^2 \right\rangle = 2K_\alpha \Delta t^\alpha, \quad (8)$$

where  $\langle \dots \rangle$  signifies the ensemble average,  $N$  is the number of observed positions per trajectory,  $K_\alpha$  is a generalized diffusion coefficient and  $\alpha$  is the anomalous diffusion exponent<sup>32</sup>. For  $\alpha = 1$ ,  $K_\alpha$  corresponds to the lateral diffusion coefficient  $D_{||2}$ , however, for  $0 < \alpha < 1$  the behavior becomes sub-diffusive. This situation is best described by a time-scale-dependent diffusion coefficient  $D_{||2,\alpha}(\Delta t) = K_\alpha \Delta t^{\alpha-1}$ .

## B. Results and Discussion

### 1. Particle height in an asymmetric slit

According to Eq. (2)-(7), the height  $h$  of the particles influences the magnitude of the hindered diffusion. To quantify the effect, we first determine the height for an individually diffusing particle from its contrast. The scatter plot in Fig. 3(a) depicts the experimentally measured and normalized contrast of such a particle for varying gap distance  $d$ .

The height of the particle in the gap relates to the contrast that is observed in iSCAT detection. For a fixed gap distance a sinusoidal dependence of the particle contrast with particle height was suggested.<sup>13</sup> The effect arises from the interference of the light scattered by the particle  $E_p$  with the background reflection, that is, the light reflected from the glass  $E_g$  and polymer/silicon interface  $E_s$ , see Fig. 3(b). As discussed in the methods section, the background reflection is also a function of the gap distance, resulting in a more complex relation of the particle contrast with gap distance. In a previous publication we showed how the effective incident angle model describing the background reflection is extended to include the particle reflection using three additional parameters to include the light scattered by a nanosphere in the nanofluidic gap.<sup>23</sup> The first and the second parameter,  $p$  and  $\phi_0$ , describe the amplitude and the accumulated phase of light scattered by the particle and collected by the camera. In addition, at the particle position, the light reflected by the substrate is reduced by a fraction  $\gamma$ . Due to the interferometric origin, the contrast of the particle is

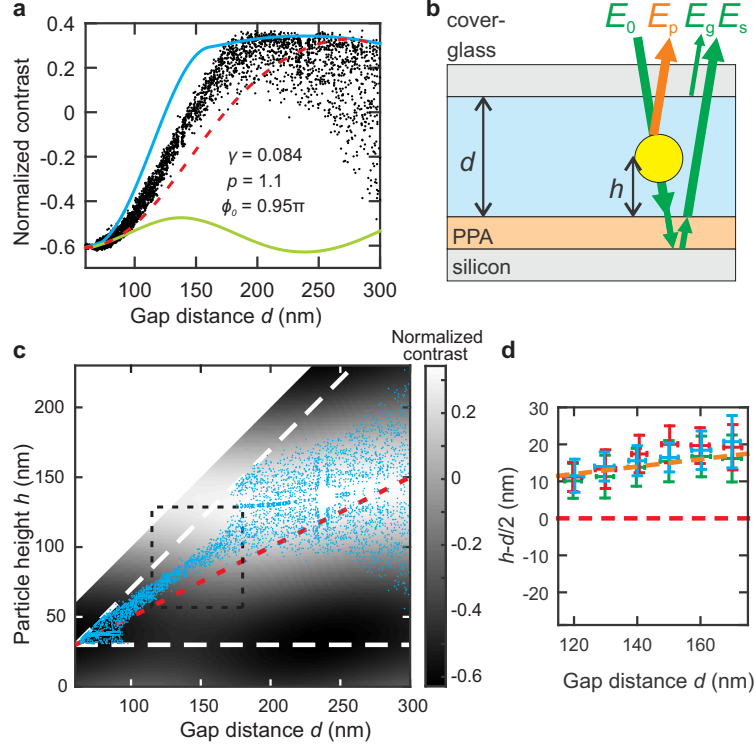


FIG. 3. (a) Contrast signal of a nanosphere (dots), a simulated particle in the middle of the gap (dashed red line) and envelopes of simulated maximum (blue line) and minimum (green line) contrast for all possible particle heights. (b) Schematic illustration of the particle at height  $h$  in a gap of size  $d$ . Incoming laser light  $E_0$  is scattered by the particle ( $E_p$ ), partially transmitted and reflected at the substrate ( $E_s$ ) and reflected by the cover glass-water surface ( $E_g$ ). (c) Attributed particle heights (blue) are obtained by matching the measured (see panel a) and simulated contrast values (gray-scale image). The confining surfaces and the particle radius restrict the possible  $h$  values (dashed white lines). The dashed red line indicates the height values corresponding to the center of the gap. (d) Deviation of the observed particle height from the gap center  $h - d/2$  for a gap distance range indicated by the dashed black box in panel c for three individually measured particles (blue, red, and green). The error bars indicate the standard deviation of  $d$  and  $h$ . Phenomenologically, the relative particle height follows  $h/d \approx 0.61$  (orange dashed line).

still a periodic function of the particle height with a period of  $\omega_L/2n_{H_2O} \approx 200$  nm, where  $\omega_L = 532$  nm is the laser wavelength and  $n_{H_2O} = 1.33$  is the refractive index of water. In the experiments, we adjusted the polymer thickness to position the minimum of the particle contrast at tight confinement of  $d \approx 70$  nm, see Fig. 3(a). Consequently, a diffusing

particle will probe the entire envelope of the contrast signal if it probes more than 100 nm of the height space above the minimum contrast position. In Fig. 3(a) the black scatter plot indeed does not rise above a particle contrast of  $\approx 0.35$  and shows a turnaround at a particle contrast of  $\approx -0.6$ . Using the optical model described in detail in Ref.<sup>23</sup> the parameters  $\gamma$ ,  $p$  and  $\phi_0$  are iteratively optimized until the envelope predicted by the model (blue and green line in Fig. 3(a)) matches the observed extremal contrast values, considering the finite range of possible particle heights given by the gap distance  $d$  and the finite radius  $a$  of the particle ( $a \leq h \leq d - a$ ). The procedure ensures that the three parameters can be obtained without the need of additional height calibration using immobilized particles.<sup>23</sup> The red line illustrates the modeled contrast of a particle positioned in the middle of the gap.

The contrast modeled as a function of gap distance  $d$  and particle height  $h$  is shown as grayscale background in Fig. 3(c). To obtain the height values (blue dots) for a measured contrast we use the simulated values for a given gap distance as a lookup table. The short illumination time of  $\lesssim 40 \mu\text{s}$  is essential to measure almost instantaneous particle heights<sup>33</sup> and to obtain reliable height-distribution data. The periodicity of the contrast signal with particle height leads to either one or multiple possible solutions for the particle height. In the single-value range of  $115 \text{ nm} \leq d \leq 175 \text{ nm}$  we determined the averaged deviation  $h - d/2$  of the particle height from the gap center (see Fig. 3(d)).

Physically, the average height of the negatively charged particles is determined by the relative repulsion of the particles from the like charged confining surfaces. A height above the center of the gap indicates a higher charge on the polymer surface, which does not contain sites that could dissociate. However, it is known that hydrophobic surfaces often attain a negative charge in contact with water, most likely due to the preferential absorption of oxianions.<sup>34</sup>

## 2. *Confined lateral diffusion of nanospheres*

To measure the lateral diffusion of nanoparticles as a function of gap distance, we exploit the high mechanical stability and tunability of the nanofluidic confinement apparatus. We vary the gap distance for different measurements and then use the feedback-control loop to keep it constant (see Fig. 2(e)) while acquiring frames for 15 s. For gap distances  $d \gtrsim 200 \text{ nm}$ , on average  $23 \pm 5$  particles per frame are detected, whereas for higher confinements

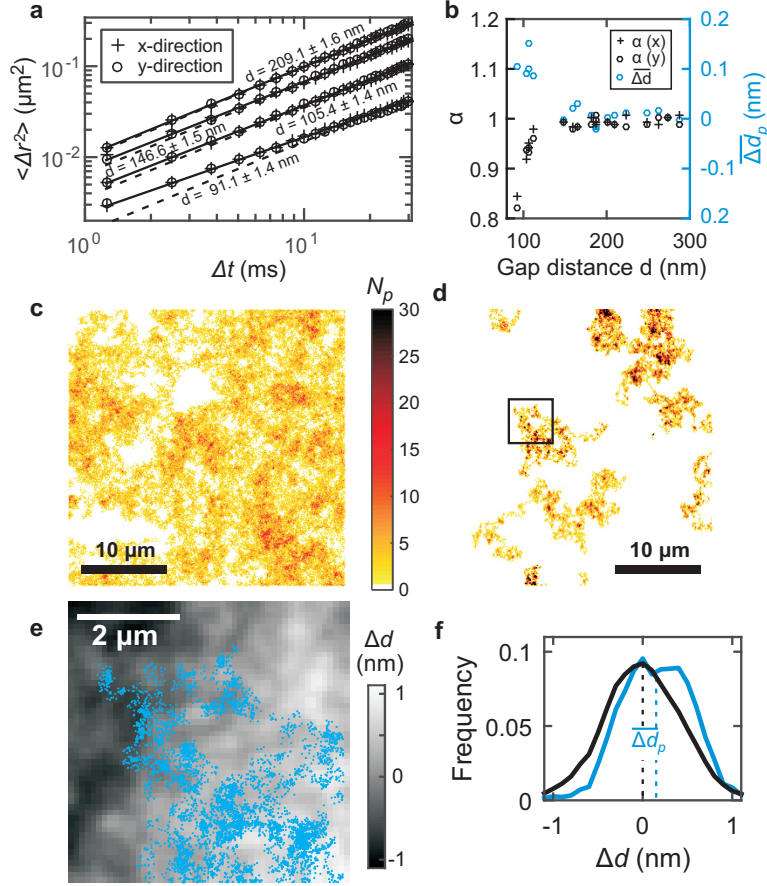


FIG. 4. (a) Measurements of the lateral MSD in the  $x$ - and  $y$ -direction at four different gap distances  $d$ . The solid and the dashed lines indicate fits of Eq. (8) to the data for anomalous and normal diffusion, respectively. (b) The parameter  $\alpha$  indicates the degree of normal diffusion  $\alpha = 1$  and sub-diffusion  $\alpha < 1$  (black symbols). An average value of the  $\overline{\Delta d_p} > 0$  (see panel f) indicates that particles avoid narrow gap regions (blue circles). (c,d) Number of detected particles  $N_p$  in a 100 nm grid during a 15 s measurement at an average gap distance of (c)  $d = 210.0 \pm 1.0$  nm and (d)  $d = 105.9 \pm 1.0$  nm. (e) Gap distance modulation  $\Delta d$  and detected particle positions (blue dots) for the area indicated by the black box in panel d. (f) Histograms of the gap distance modulation (black line) and for the locations of the gap distance modulation sampled by the particles (blue line).

with  $d \lesssim 200$  nm only  $8 \pm 3$  particles are detected. The high frame rate (800 FPS) nevertheless provides a sampling of 60,000 up to 300,000 particle positions for each measurement.

For each gap distance  $d$ , we obtain the one-dimensional (1D) time and ensemble averaged

MSD for a range of time steps  $\Delta t$  from  $1.25 \leq \Delta t \leq 31.25$  ms, see Fig. 4(a). A strong decrease of the diffusivity with decreasing gap distance is apparent. Fits of Eq. (8) to the MSD in the  $x$ - and  $y$ -directions are given as solid lines. The dashed lines indicate fits to the data for normal diffusion ( $\alpha = 1$ ). The fit parameter  $\alpha$  indicating sub-diffusion for  $\alpha < 1$  is shown in Fig. 4(b). At a confinement  $d < 120$  nm, a scale-dependent diffusion coefficient is observed, see also the increasing deviation of the dashed and solid lines in Fig. 4(a). This effect has been attributed to the presence of lateral obstacles preventing a free diffusion of the particles.<sup>35</sup> In our case however, these obstacles are either induced by local charge inhomogeneities or by the roughness of the confining walls.

We use a simple picture to assess this hypothesis. In the so called linear superposition approximation the interaction energy  $U(h)$  of a charged spherical particle at a distance  $h$  to a charged plane is given by:<sup>23,36</sup>

$$U(h) = 4\pi\epsilon\epsilon_0 a \psi_{P,eff} \psi_{S,eff} e^{-\kappa(h-a)}, \quad (9)$$

where  $\kappa^{-1}$  is the Debye length,  $\epsilon$  is the dielectric constant of the medium,  $\epsilon_0$  is the vacuum permittivity,  $a$  is the radius, and  $\psi_{P,eff}$  and  $\psi_{S,eff}$  are the effective surface potentials of plane and sphere, respectively. In this linear approximation the overall interaction energy of a sphere between two walls is obtained by the sum of the interaction energies to each wall. Assuming a surface potential of the sphere of  $-58$  mV (see methods) and a surface potential of the walls of  $-67$  mV as determined in our previous experiments<sup>23</sup>, we obtain a change in interaction energy of  $\approx 0.8 k_B T$  for a gap distance of  $120$  nm and a gap distance modulation of  $1$  nm. The simple model corroborates the interpretation that the observed RMS roughness of the glass of  $0.4$  nm provides significant energy barriers for diffusion. We note, however, that the same effect could be induced by a charge modulation of the surface potential (or correspondingly the surface charge) by  $\approx 5\%$ .

To further investigate the origin of the obstacles we analyzed the time-averaged lateral particle distribution and its correlation to the measured locally resolved gap distance variation  $\Delta d$  (see Fig. 2d). To obtain a measure for the particle distribution, we divide the field of view into a  $100$  nm grid and count the total number of particles visiting each grid section for all frames. The resulting number of detected particles is visualized as "heatmaps" in Fig. 4(c,d) for an average gap distance of (c)  $d = 209.1 \pm 1.0$  nm and (d)  $d = 105.4 \pm 1.0$  nm. The particles are quasi uniformly distributed over the entire field of view for the larger separation

and are more localized in the narrower slit.

In order to correlate the detected particle trajectories with the gap distance modulation  $\Delta d$ , see Fig. 2(d), we have to compensate for the tilt in the gap distance map. We divide the map into squares of  $5 \times 5 \mu\text{m}^2$  size, roughly corresponding to the 1D diffusion length during the measurement of  $r_{\text{diff}} \approx 5 \mu\text{m}$ , and correct for the offset in local gap distance modulation  $\Delta d$  for each square. For example, Fig. 4(e) shows  $\Delta d$  and the positions of a single diffusing particle (blue dots) for the square given by the box in Fig. 4(d). According to this trace the particle samples certain locations of the  $\Delta d$  map and we term the range of sampled values  $\Delta d_p$ . The average histograms of  $\Delta d$  and  $\Delta d_p$  for all squares are shown in Fig. 4(f) as black and blue lines, respectively. Clearly, the particles prefer to be located at a position having a larger gap distance as apparent by the shift of the  $\Delta d_p$  histogram to more positive  $\Delta d$  values. To obtain a qualitative measure of the strength of this effect, we determined the distance of the center of mass of the two histograms  $\overline{\Delta d_p}$  for all measured gap distances, see Fig. 4(f). The result is given in Fig. 4(b) by the blue circles. For gap distances below  $d = 120 \text{ nm}$ , a significant shift of the particle position into high-gap-distance positions is apparent. This behavior is qualitatively similar to the onset of sub-diffusion measured for the MSD. Therefore we conclude that the sub-diffusion is indeed caused by the fact that the particles start to avoid regions with narrower gap distances.

Now we turn to the central result, the gap-distance-dependent lateral diffusion coefficient  $D_{||2}(d)$ , which is depicted in Fig. 5. The black scatter plot indicates the values for normal diffusion  $D_{||2,\alpha=1}(d)$  corresponding to the dashed lines in Fig. 4(a). For  $d < 120 \text{ nm}$  sub-diffusion is significant and a single diffusion coefficient is not sufficient to describe the process, see Eq. (8). Instead, the diffusion coefficient  $D_{||2,\alpha}(d, \Delta t)$  becomes dependent on the time interval  $\Delta t$ . The range for  $D_{||2,\alpha}(d, \Delta t)$  for  $1.25 \text{ ms} < \Delta t < 31.25 \text{ ms}$  is indicated for  $d < 120 \text{ nm}$  by the blue bars.

For comparison, the predicted diffusion coefficients accounting for hydrodynamic hindrance from two walls are shown for the LSA [Eq. (6) (solid lines)] and CSA [Eq. (7) (dashed lines)]. Both approximations were calculated for a particle diffusing at a measured height  $h = 0.61d$  (black) and in the middle of the slit  $h = 0.5d$  (gray). The asymmetric height leads to merely 1.5% lower diffusion coefficients and cannot explain the 20 – 50 % lower diffusivity measured. We also exclude that the localization due to surface roughness is the predominant factor for this reduction, because pronounced sub-diffusion is only observed



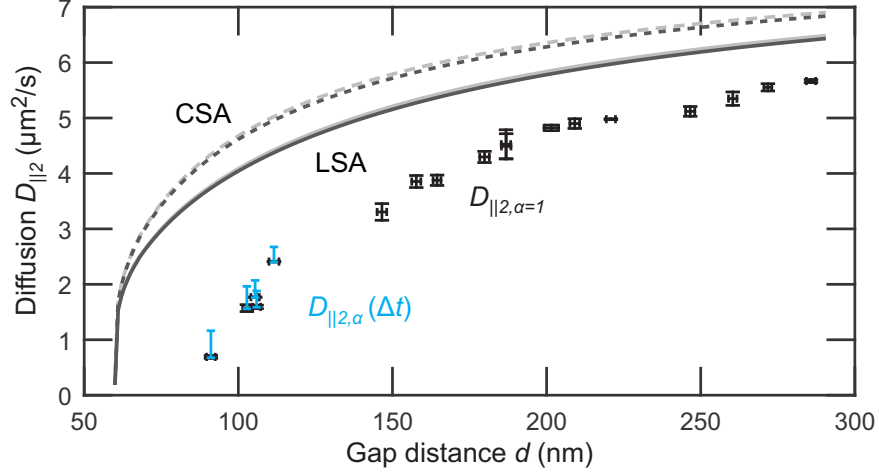


FIG. 5. Lateral diffusion coefficients for varying gap distance in a nanofluidic slit. The error of the normal diffusion coefficients  $D_{||2}$  (black scatter plot) and  $d$  are determined by the difference of  $D_{||2}$  in x and y direction and the standard deviation of  $d$ , respectively. The range of time dependent diffusion coefficients  $D_{||2,\alpha}(\Delta t)$  for  $1.25 \text{ ms} < \Delta t < 31.25 \text{ ms}$  is plotted for  $d < 120 \text{ nm}$  (blue bars). For greater gap distances the range of  $D_{||2,\alpha}(\Delta t)$  is less than 8% of the normal diffusion coefficient. Theoretically predicted diffusion coefficients by LSA (solid lines, Eq. 6) and CSA (dashed lines, Eq. 7) are shown for an average particle height at  $h = 0.5d$  (gray) and  $h = 0.61d$  (black).

for gap distances of  $d < 120 \text{ nm}$ .

In bulk, the electroviscous effect is attributed to the surface charge of the particles and leads to an increased effective viscosity and thus to a reduction in particle diffusion.<sup>37</sup> A similar mechanism should also play a role in a nanofluidic system, in particular when a particle is close to a charged wall. Whereas diffusion measurements for uncharged particles<sup>15</sup> and for particles in electrolyte with higher ionic concentration<sup>33</sup> are in agreement with predictions that consider only a hydrodynamically hindered drag. There is considerable evidence of an increased drag of charged particles near charged walls in a weak electrolyte.<sup>18,38</sup> In a similar experimental configuration Eichmann *et al.*<sup>18</sup> measured a  $\approx 30\%$  ( $\approx 55\%$ ) lower lateral diffusion coefficient for 60 nm (100 nm) gold nanospheres with a relative radius of  $\kappa a \approx 0.9$  ( $\kappa a \approx 2.1$ ) and a relative glass-particle distance of  $\kappa h - \kappa a \approx 4.5$  ( $\kappa h - \kappa a \approx 3.6$ ). These values are in agreement with the  $\approx 45\%$  lower diffusion we measure for  $\kappa a \approx 3.4$  and  $\kappa h - \kappa a \approx 4$ .

## IV. CONCLUSION

We have developed a new versatile setup for investigating the behavior of nano-objects in a tunable confinement between two surfaces. The interferometric detection setup allows us not only to detect the nano-objects with high sensitivity, but also to determine the 3D particle position and the wall separation *in situ* with nanometer spatial and millisecond temporal precision. Furthermore, a diffraction limited resolved map of the sub-nanometer-resolved gap distance can be obtained. We use the tool to measure the height and diffusion of 60 nm gold spheres as a function of absolute gap distance between a glass and a polymer surface. We find that the particles localize more closely to the glass interface indicating a higher charge of the polymer surface. Sub-diffusion becomes significant at gap distances below  $d = 120$  nm. We demonstrate that this scale dependent diffusion is correlated to particle trajectories that avoid regions of narrow gap distances caused by the surface roughness of the confining surfaces. The measured lateral diffusion coefficients are 20 – 50 % lower than predicted by purely hydro-dynamical hindrance, also when taking their asymmetric position in the gap into account. Similarly, the observed scale dependent diffusion cannot account for the effect because it is only significant for small gap distances. We conclude that electro-viscous effects are the main cause for the observed reduction in diffusivity. Our measurements provide a detailed information on the gap-distance-dependent particle diffusion, which may form the basis for testing theories describing the electro-viscous effect. In general, the results shown here demonstrate the versatility of the tool which allows one to measure nano-particle behavior as a function of confinement in remarkable detail.

## ACKNOWLEDGMENTS

The authors thank U. Drechsler, M. Sousa, and S. Reidt for technical support, C. Bolliger for proof-reading, and U. Duerig and M. Krishnan (University of Zurich) for fruitful discussions. Funding has been provided by the European Research Council StG no. 307079.

## REFERENCES

- <sup>1</sup>B. Regner, D. Vucinic, C. Domnisoru, T. Bartol, M. Hetzer, D. Tartakovsky, and T. Sejnowski, *Biophys. J.* **104**, 1652 (2013).

- <sup>2</sup>M. Baum, F. Erdel, M. Wachsmuth, and K. Rippe, Nat. Commun. **5**, 4494 (2014).
- <sup>3</sup>R. Langer and N. A. Peppas, AIChE Journal **49**, 2990 (2003).
- <sup>4</sup>T. Gong, D. T. Wu, and D. W. M. Marr, Langmuir **18**, 10064 (2002).
- <sup>5</sup>A. Reinmüller, E. C. Oğuz, R. Messina, H. Löwen, H. J. Schöpe, and T. Palberg, J. Chem. Phys. **136**, 164505 (2012).
- <sup>6</sup>L. R. Huang, E. C. Cox, R. H. Austin, and J. C. Sturm, Science **304**, 987 (2004).
- <sup>7</sup>M. Grzelczak, J. Vermant, E. Furst, and L. Liz-Marzán, ACS Nano **4**, 3591 (2010).
- <sup>8</sup>L. Bocquet and P. Tabeling, Lab on a Chip **14**, 3143 (2014).
- <sup>9</sup>R. J. Hunter and L. R. White, *Foundations of colloid science* (Clarendon Oxford, 1987).
- <sup>10</sup>A. Dhinojwala and S. Granick, The Journal of chemical physics **107**, 8664 (1997).
- <sup>11</sup>C. Clasen and G. H. McKinley, Journal of non-newtonian fluid mechanics **124**, 1 (2004).
- <sup>12</sup>J. N. Israelachvili, *Intermolecular and Surface Forces* (Academic Press, London, 1992).
- <sup>13</sup>M. Krishnan, N. Mojarad, P. Kukura, and V. Sandoghdar, Nature **467**, 692 (2010).
- <sup>14</sup>J. Tae Kim, S. Spindler, and V. Sandoghdar, Nat. Commun. **5**, 3380 (2014).
- <sup>15</sup>B. Lin, J. Yu, and S. A. Rice, Phys. Rev. E **62**, 3909 (2000).
- <sup>16</sup>E. R. Dufresne, D. Altman, and D. G. Grier, EPL (Europhysics Letters) **53**, 264 (2001).
- <sup>17</sup>N. Kaji, R. Ogawa, A. Oki, Y. Horiike, M. Tokeshi, and Y. Baba, Anal. Bioanal. Chem. **386**, 759 (2006).
- <sup>18</sup>S. L. Eichmann, S. G. Anekal, and M. A. Bevan, Langmuir **24**, 714 (2008).
- <sup>19</sup>L. Zhao, Y. Zhong, Y. Wei, N. Ortiz, F. Chen, and G. Wang, Anal. Chem. **88**, 5122 (2016).
- <sup>20</sup>V. Jacobsen, P. Stoller, C. Brunner, V. Vogel, and V. Sandoghdar, Opt. Express **14**, 405 (2006).
- <sup>21</sup>P. Kukura, Nat. Methods **6**, 923 (2009).
- <sup>22</sup>N. Mojarad, V. Sandoghdar, and M. Krishnan, Opt. Express **21**, 9377 (2013).
- <sup>23</sup>S. Fringes, M. Skaug, and A. W. Knoll, J. Appl. Phys. **119**, 024303 (2016).
- <sup>24</sup>H. Zhu, M. Holl, T. Ray, S. Bhushan, and D. R. Meldrum, Journal of Micromechanics and Microengineering **19**, 065013 (2009).
- <sup>25</sup>G. Frens, Nature **241**, 20 (1973).
- <sup>26</sup>R. Parthasarathy, Nat. Methods **9**, 724 (2012).
- <sup>27</sup>Y. Pawar and J. L. Anderson, Indust. & Engin. Chem. Res. **32**, 743 (1993).
- <sup>28</sup>H. Faxèn, Ark. Mat. Astron. Fys. **17** (1923).

- <sup>29</sup>A. Goldman, R. Cox, and H. Brenner, *Chemical Engineering Science* **22**, 637 (1967).
- <sup>30</sup>C. W. Oseen, *Neuere Methoden und Ergebnisse in der Hydrodynamik* (Akademische Verlagsgesellschaft, Leipzig, 1927).
- <sup>31</sup>L. Lobry and N. Ostrowsky, *Phys. Rev. B* **53**, 12050 (1996).
- <sup>32</sup>R. Metzler and J. Klafter, *Physics reports* **339**, 1 (2000).
- <sup>33</sup>S. L. Eichmann and M. A. Bevan, *Langmuir* **26**, 14409 (2010).
- <sup>34</sup>C. Tian and Y. Shen, *Proc. Natl. Acad. Sci. USA* **106**, 15148 (2009).
- <sup>35</sup>G. Volpe, G. Volpe, and S. Gigan, *Sci. Reports* **4**, 3936 (2014).
- <sup>36</sup>Z. Adamczyk and P. Warszyński, *Adv. Colloid Interface Sci.* **63**, 41 (1996).
- <sup>37</sup>B. Conway, A. Dobry-Duclaux, and F. Eirich (Academic Press New York and London, 1960) p. 83.
- <sup>38</sup>M. D. Carbajal-Tinoco, G. Cruz de León, and J. L. Arauz-Lara, *Phys. Rev. E* **56**, 6962 (1997).
- <sup>39</sup>S. M. Görisch, M. Wachsmuth, C. Ittrich, C. P. Bacher, K. Rippe, and P. Lichter, *Proc. Nat. Acad. Sci. (USA)* **101**, 13221 (2004).
- <sup>40</sup>A. Mukhopadhyay, J. Zhao, S. C. Bae, and S. Granick, *Physical review letters* **89**, 136103 (2002).
- <sup>41</sup>D. Pires, J. L. Hedrick, A. De Silva, J. Frommer, B. Gotsmann, H. Wolf, M. Despont, U. Duerig, and A. W. Knoll, *Science* **328**, 732 (2010).